

Carrier-Aided Dual-Frequency Vectorized Tracking Architecture for NavIC Signals

Abhijit Dey¹, Member, IEEE, Kaushik Iyer², Bing Xu³, Member, IEEE,
Nitin Sharma⁴, and Li-Ta Hsu⁵, Member, IEEE

Abstract—A new carrier-aided dual-frequency vectorized tracking (CA-DFVT) architecture for the Navigation with Indian Constellation (NavIC) is presented. CA-DFVT tracks both NavIC L5 (1176.45 MHz) and S-band (2492.028 MHz) signals concurrently. It uses the precise carrier phase measurements from the S-band signal and the unambiguous code phase measurements from the L5 signal to form a new measurement model for the extended Kalman filter (EKF) to estimate the position, velocity, and time (PVT) solutions. The new measurement model takes advantage of the benefits of the higher frequency S-band signal, i.e., less ionospheric delay and carrier phase noise, as well as the L5 signal's inherent noise mitigation capabilities. Compared to the single-frequency approach, the dual-frequency approach in CA-DFVT eliminates the ionospheric effect and minimizes other errors, resulting in better navigation solutions. The proposed CA-DFVT enhances the reliability and robustness of NavIC signal tracking and position estimation in interference and high dynamics environments. We used static and dynamic field tests to validate the performance and robustness of the proposed CA-DFVT receiver architecture. In comparison to single-frequency (L5/S-band) vector tracking, the CA-DFVT receiver demonstrated consistent signal tracking and position estimation with higher position accuracy. In the static case, the mean horizontal position accuracy of CA-DFVT improves by approximately 2–4 and 9–14 m compared to L5-only VT and S-only VT, respectively, while, in the dynamic case, it improves by approximately 2–5 and 25–42 m, respectively.

Index Terms—Carrier phase, extended Kalman filter (EKF), interference, Navigation with Indian Constellation (NavIC), vector tracking (VT).

I. INTRODUCTION

THE Indian Regional Navigation System (IRNSS), with its operational name as the Navigation with Indian

Manuscript received October 11, 2021; revised December 20, 2021; accepted January 9, 2022. Date of publication January 27, 2022; date of current version February 25, 2022. This work was supported in part by The Hong Kong Polytechnic University Exchange Student Fellowship Program and in part by the Universal Software Radio Peripheral (USRP)-2932 devices used as radio frequency (RF) front-end were purchased under the contingency fund of the Indian Space Research Organisation (ISRO) Research Sponsored (RESPOND) Project under Grant ISRO/RES/3/720/2016-17. The Associate Editor coordinating the review process was Jingyu Hua. (*Corresponding author: Bing Xu.*)

Abhijit Dey is with the Department of Electrical and Electronics Engineering, Birla Institute of Technology and Science, Pilani, K K Birla Goa Campus, Pilani 403726, India, and also with the Department of Aeronautical and Aviation Engineering, The Hong Kong Polytechnic University, Hong Kong, SAR, China (e-mail: abhijitdey89@gmail.com).

Kaushik Iyer is with the Department of Electrical Engineering, Arizona State University, Tempe, AZ 85281 USA (e-mail: kiyer2396@gmail.com).

Nitin Sharma is with the Department of Electrical and Electronics Engineering, Birla Institute of Technology and Science, Pilani, K K Birla Goa Campus, Pilani 403726, India (e-mail: nitinn@goa.bits-pilani.ac.in).

Bing Xu and Li-Ta Hsu are with the Department of Aeronautical and Aviation Engineering, The Hong Kong Polytechnic University, Hong Kong, SAR, China (e-mail: pbing.xu@polyu.edu.hk; lt.hsu@polyu.edu.hk).

Digital Object Identifier 10.1109/TIM.2022.3146927

Constellation (NavIC), is an autonomous system developed by the Indian Space Research Organisation (ISRO) that provides precise navigation solutions within 1500 km of the Indian subcontinent [1]. NavIC is fully operational and transmits signals on L5 (1176.45 MHz) and S-band (2492.028 MHz) frequencies. Today, NavIC is nearly ubiquitous for civil and military users, enabling the design and development of various NavIC-based instrumentation and measurement applications [2]. These applications demand accurate and precise navigation and timing information. However, in environments such as high dynamics, weak signal strength, and interference, the conventional scalar tracking (ST)-based global navigation satellite system (GNSS) receiver architecture results in inaccurate positioning. This is due to the decentralized architecture of the conventional ST-based receiver, which uses independent tracking loops to track the GNSS signals from each satellite. As such, advanced algorithms and architectures are required to support accurate and robust positioning in harsh scenarios. In this regard, numerous techniques, such as multiantenna design [3], algorithm enhancement [4], [5], and external aids (i.e., INS/GNSS) [6], have been widely developed and applied in GNSS. Among these strategies, the vector tracking (VT) technique is the most widely used in GNSS receivers due to its low cost and ease of implementation [7]. In VT, the satellite signals are tracked by the Kalman filter, which combines the tasks of signal tracking and navigation solving into a single algorithm. This enables remarkable improvement in the performance of GNSS signal processing in challenging environments. Over recent years, the advantages of VT over conventional ST have been exploited and proved in many challenging scenarios, such as non-line-of-sight (NLOS) signals [8], weak signals and high receiver dynamics [5], [9], multipath and ionospheric scintillation [10], and contaminated signal conditions [4], [11].

As mentioned earlier, as the NavIC system evolves, an increasing number of NavIC-based applications are being designed and developed. These applications require precise and accurate navigation solutions for performing dedicated tasks. However, recent studies have revealed that the NavIC S-band signal is susceptible to unlicensed S-band sources, such as wireless fidelity (Wi-Fi)/IEEE 802.11 Standard, long-term evolution (LTE), and Bluetooth [12], [13]. Moreover, it is evident that high-frequency S-band signals are naturally more affected by interference and multipath than L-band signals [14]. As a result, standalone NavIC S-band signal-based navigation solutions will eventually be disturbed by the environment, resulting in erroneous and inaccurate positioning [15]. On the contrary, it is also true that the higher

frequency will have a less ionospheric impact. Therefore, the NavIC S-band signals are less prone to ionospheric effect, and also, due to high frequency, the carrier phase noise is less compared to other GNSS signals. In addition, navigational solutions based only on pseudorange and pseudorange rate measurements, also referred to as code signals, provide mediocre position accuracy. Thus, GNSS receivers can also use carrier signals estimated as carrier phase measurements, which are significantly more precise. This certainly motivated us to exploit the benefits of higher frequency S-band and L5 signals to design an architecture that combines both code and carrier phase measurements. The idea is to enhance the receiver robustness in high dynamics and interference conditions while, at the same time, reducing the architecture complexity and conserving the low-cost feasibility criteria of the NavIC receiver.

A. Related Work

The initial concept related to vector delay-locked loop (VDLL) was presented in [16], where the code tracking is done in the vector mode, while the carrier tracking is accomplished similar to a conventional receiver. Over the last several years, VT has piqued the interest of a large number of researchers with the goal of enhancing a receiver's ability to track weak signals in dynamic environments [9], [17], interference antijamming [18], ionospheric scintillation [10], and multipath and NLOS [7], [8]. Most of these receiver architectures deal with the single-frequency VT approach. For instance, Xu and Hsu [7] presented a self-developed global positioning system (GPS) L1 software receiver based on VDLL, where the main focus was on the code measurements of the incoming signal. Zhao and Akos [19] presented an open-source code of vector delay/frequency-locked loop (VDFLL) based on a GPS software receiver initially developed by Borre *et al.* [20]. In this article, the authors presented the performance assessment of the VT loop by comparing it with that of the traditional ST loop, where the navigation solution was estimated using the traditional iterative least-squares method. Although most of these techniques try to address the problems associated with challenging environments, the majority of them mainly focus on VT for the single-frequency-receiver architecture. Moreover, very limited work has been done so far in multifrequency VT, despite the several benefits of the multifrequency approach [21]. The related literature for various VT techniques developed so far is summarized in Table I. Broadly, these are divided into three categories i.e., single-constellation single-frequency, multiconstellation single-frequency, and multiconstellation dual-frequency/multifrequency.

VT-based architectures rely on the extended Kalman filter (EKF) for better performance, and since the EKF depends on accurate measurements for better estimations, the existing single-frequency VT architectures were modified and incorporated into multiconstellation systems [26]. Tabatabaei *et al.* [24] presented a receiver architecture that integrates measurements from GPS and GLONASS in VT

TABLE I
LITERATURE SURVEY ON VT-BASED RECEIVER ARCHITECTURE DESIGN

Architecture Types	Application/Purpose
Single-Constellation Single-Frequency VT	High user dynamics [9], contaminated or isolated signals [4] under jamming scenarios [22], NLOS correction and mitigation [8], Performance of VDFLL architecture over ST [19], VDFLL under ionospheric scintillation [10], adaptive VT [23], interference detection and mitigation NavIC VT [15]
Multi-Constellation Single-Frequency VT	GPS + GLONASS [20], [24], [25], GPS + Galileo for multipath and ionospheric error correction [26], [27]
Multi-Constellation Dual/Multi-Frequency ST	GPS + GLONASS dual-frequency [28], multi-constellation multi-frequency [29]

mode. The idea was to combine two distinct constellations in order to increase the number of satellites for a given epoch. As a result, the number of measurements available to EKF increased, and hence, the overall receiver performance improved. This approach provided better positioning results in situations, such as signal blockage and urban canyons [25]. Based on a similar concept, a modified VDFLL-based architecture combining GPS and Galileo was presented in [27]. The main focus was to provide accurate positioning solutions under multipath and ionospheric scintillation scenarios [30].

An alternative approach for improving the positioning is to employ signals from multiple frequencies [21], [31], as signals of varying frequencies have different signal properties. For instance, the L5-based receiver offers advantages in terms of interference immunity to 2G/3G/4G/5G and Wi-Fi/Bluetooth [15]. This is due to the fact that the new and modernized signals in the L5-/E5a-band have inherent noise and multipath mitigation capabilities [32]. These capabilities of L5/E5a when combined with the ability of eliminating ionospheric effect using dual-frequency, significant improvements in both measurement and positioning accuracy can be achieved. On the other hand, higher frequency S-band signals have less ionospheric delay [33]. Therefore, a higher frequency S-band signal when used in combination with L1 or L5 provides better position accuracy [14], [34]. Benefits of combining L + S than L + L in the removal of ionospheric errors have been presented in [14]. A dual-frequency (L1/L2) GPS VT-based software receiver implemented in [35] showed the superior performance of a dual-frequency architecture in removing ionospheric errors compared to a single-frequency receiver. The superior performance is because of the usage of differential measurements by the dual-frequency receiver architecture. Furthermore, this concept was extended to multifrequency multiconstellation receiver architecture in order to exploit differential measurements [22], [28], [29] while, at the same time, increasing the satellite availability too. This approach helped in improving the positioning performance of the receiver in two ways; first, it increased the number of satellites; second, the signal properties are utilized to tackle the challenging environmental conditions.

B. Our Approach and Contribution

In this article, we propose a carrier-aided dual-frequency VT (CA-DFVT) receiver architecture to enhance the reliability and robustness of NavIC signal tracking and navigation solution estimation. CA-DFVT jointly tracks NavIC L5 and S-band received signals. The following key parameters make the proposed CA-DFVT receiver architecture different from existing approaches.

- 1) Unlike the single-frequency receiver architectures, the CA-DFVT receiver architecture jointly tracks two different bands i.e., L5 and S, and performs position estimation using a feedback loop using an EKF.
- 2) Unlike other VT receiver architectures, the CA-DFVT receiver uses the carrier phase measurements from S-band and code phase measurements from L5 to formulate new pseudorange measurements for the EKF. In high dynamics, the code tracking loop is not very sensitive to changes in receiver dynamics. Therefore, instead of modifying the code tracking loop, we rather use carrier phase measurements to assist the code tracking. Thus, a new measurement model is proposed, which combines the carrier phase measurements and code phase measurements to generate new pseudorange and pseudorange rate measurements.
- 3) Despite using single-frequency Klobuchar [36] or grid-based ionospheric corrections [37], ionospheric residual errors remain in the pseudoranges. However, using two different frequencies from the same satellite enables the usage of difference equations in pseudorange estimates and, thus, helps in removing the ionospheric errors and cycle slips [38]. Unlike, other VT receiver architectures, the proposed CA-DFVT uses the combined measurements from L5 and S-band for the EKF, which cancels out the ionosphere's effect and minimizes the effect of other errors on the observations. Finally, because of the coupled structure of CA-DFVT, any disadvantages of a specific frequency band that may exist in specific environments are minimized.

In addition, two experimental tests were conducted, which includes one static and one dynamic open sky test to evaluate the proposed CA-DFVT receiver architecture performance. We selected reliability and robustness as critical performance criteria:

- 1) consistent and accurate NavIC signal tracking and position estimation during stationary and interference conditions;
- 2) position accuracy in low latitude ionospheric and dynamic effects, respectively.

The rest of this article is organized as follows. In Section II, the proposed CA-DFVT receiver architecture is described in detail. Section III discusses the software implementation and experimental setup. The experimental results are discussed in Section IV. Section V summarizes this article.

II. CARRIER-AIDED DUAL-FREQUENCY VECTORIZED TRACKING (CA-DFVT) ARCHITECTURE

In the proposed CA-DFVT architecture, the conventional ST is used to process the IF signal and decode the ephemeris data, where the acquisition of NavIC L5 and S-band signals are done separately. The position, velocity, and time (PVT) calculated using the conventional ST is used to initialize the VT of CA-DFVT, which takes place in an integrated manner. For the tracking architecture of our CA-DFVT, we used the noncoherent VDFLL proposed in [19] and [39]. We first developed and implemented it for NavIC single-frequency [15] and then modified the entire tracking loop with our CA-DFVT. As described earlier, the main innovation is the formulation of a new measurement model in CA-DFVT, which utilizes the carrier phase measurements from the S-band and aids the code phase measurements of L5 to form new pseudorange measurements. In CA-DFVT, the code phase error and the frequency error from the L5 tracking loop and only the frequency error from the S-band tracking loop are used to form the new measurement model. Detailed derivation and explanation of the new measurement model are presented in Section II-A. Finally, these measurements are fed to the EKF, which computes the user PVT and simultaneously uses them to update the code and carrier numerically control oscillator (NCO) for all channels. The tracking architecture of the CA-DFVT receiver architecture is shown in Fig. 1.

VT is initialized using an estimate of the receiver position ($\mathbf{p} = [x, y, z]^T$) in meters, receiver velocity ($\mathbf{v} = [v_x, v_y, v_z]^T$) in meters/second, and receiver clock bias (b) in meters and drift (\dot{b}) in meters/second [19]. The superscript T denotes the transpose operator. These initial estimates are obtained from the ST results. The estimated receiver position and velocity equations at the next epoch are given as follows:

$$\begin{aligned}\hat{\mathbf{p}}_{k+1} &= \hat{\mathbf{p}}_k + \Delta t_k \hat{\mathbf{v}}_k \\ \hat{\mathbf{v}}_{k+1} &= \hat{\mathbf{v}}_k\end{aligned}\quad (1)$$

where $\Delta t_k = t_{k+1} - t_k$ and $\hat{\mathbf{p}}$ denotes an estimate of \mathbf{p} . Since acceleration is not given as input, the velocity propagation is modeled only by the addition of noise to the previous epoch. The propagation equations for the receiver clock bias and clock drift are given as follows:

$$\begin{aligned}\hat{b}_{k+1} &= b_k + \Delta t_k \cdot \delta \dot{b}_k \\ \hat{\dot{b}}_{k+1} &= \dot{b}_k + \delta \dot{b}_k\end{aligned}\quad (2)$$

where “ δ ” represents an error term. If receiver position and velocity error are defined as $\delta \mathbf{p}_k = \mathbf{p}_k - \hat{\mathbf{p}}_k$ and $\delta \mathbf{v}_k = \mathbf{v}_k - \hat{\mathbf{v}}_k$, respectively, then, the code phase error ($\Delta \tau$) and frequency error (Δf) from the discriminators for the k th epoch and the j th satellite are related to the receiver position and velocity as follows:

$$\begin{aligned}\Delta \tau_{\rho,k}^j &= \Delta \tau_k^j \cdot \lambda_{\text{code}} \\ &= \delta b_k + (\delta \mathbf{p}_k^T) \mathbf{a}_k^j + \eta_{\text{code}}^j \\ \Delta f_{\rho,k}^j &= \Delta f_k^j \cdot \lambda_{\text{carr}} \\ &= \delta \dot{b}_k + (\delta \mathbf{v}_k^T) \mathbf{a}_k^j + \eta_{\text{carr}}^j\end{aligned}\quad (3)$$

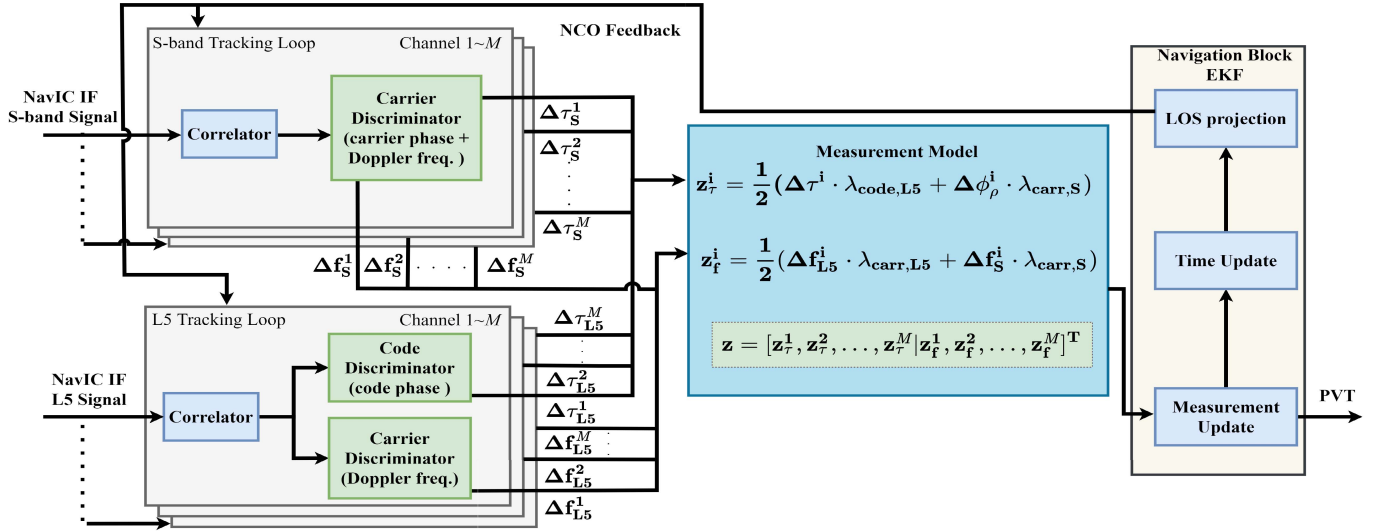


Fig. 1. Tracking architecture of the proposed CA-DFVT.

where $\Delta\tau_{\rho,k}^j$ is in meter and $\Delta f_{\rho,k}^j$ is in meters/second. $\lambda_{\text{code}} = c/f_{\text{code}}$, where f_{code} is the code frequency. $\lambda_{\text{carr}} = c/f_{\text{carr}}$, where f_{carr} is the carrier frequency. \mathbf{a}^j is the 3-D line of sight (LOS) unit column vector for the j th satellite, and η is the discriminator noise. Detailed derivation of (3) is given in the Appendix. These $\Delta\tau_k^j$ and Δf_k^j are used to update the NCO to obtain the true receiver position and velocity at epoch k th [4], [19].

A. Proposed Measurement Model

The code phase and carrier frequency residuals measured by the code and carrier discriminators, as given in (3), are used as input to the EKF for the measurement update at epoch k . These residuals are first translated into code and carrier phase measurements and then used to formulate a new measurement model, which combines both code and carrier. Carrier phase measurements are more precise than code phase measurements and can be used to determine distances. However, due to integer ambiguity, carrier phase measurements cannot be employed directly. However, if phases are computed relative to the same point, the integer ambiguity of different measurement epochs will remain constant.

Ideally, the mathematical model of the pseudorange equation without any error term is expressed as [40]

$$\rho_I(t) = R + c(b_r - b_s) \quad (4)$$

where R is the geometric range, b_r is the receiver clock bias in seconds, b_s is the satellite clock bias in seconds, and c denotes the speed of light.

However, when the GNSS signals travel through the ionosphere and troposphere, refraction takes place. The ionosphere is a dispersive medium i.e., its refractive index is a function of frequency. Moreover, the effect of the ionosphere on the code and the carrier phase measurements have opposite polarities. On the other hand, the troposphere is not a dispersive medium, and its effect remains the same for both code and carrier phase measurements.

Now, including the ionospheric and tropospheric effects, the pseudorange equation is given as [38]

$$\begin{aligned} \rho(t) &= R + c \cdot (b_r - b_s) + I(t) + T_r(t) + \eta \\ &= \rho_I(t) + I(t) + T_r(t) + \eta \end{aligned} \quad (5)$$

where $I(t)$ and $T_r(t)$ are the ionospheric and tropospheric effects, respectively, and η includes any unaccounted errors.

The instantaneous value of carrier phase $[\phi(t)]$ used here is obtained using carrier discriminator. We first obtain the instantaneous Doppler frequency from the discriminator and then integrate it over one measurement epoch to get the carrier phase in radians. The carrier phase measurement $[\phi_\rho(t)]$ equation in meters is, thus, given as

$$\begin{aligned} \phi_\rho(t) &= \lambda \cdot \phi(t) \\ &= R + c(b_r - b_s) - I(t) + T_r(t) + \lambda N(t) + \eta_\phi \\ &= \rho_I(t) - I(t) + T_r(t) + \lambda \cdot N(t) + \eta_\phi \end{aligned} \quad (6)$$

where $\lambda = c/f$ is the wavelength of the transmitted signal, f denotes the carrier frequency, and $N(t)$ is the integer phase ambiguity term, which is ideally a constant, but, under the condition of cycle slips, it is a piecewise function of time. η_ϕ is the noise associated with the carrier phase measurement, which is generally in centimeters. Note that (6) is the new pseudorange equation and is consistent with that in (5) except for the polarity of the ionospheric term.

The code discriminator output $[\Delta\tau(t)]$ in meter is given as

$$\Delta\tau_\rho(t) = \Delta\tau(t) \cdot \lambda = \delta\rho_I(t) + \delta I(t) + \delta T_r(t) + \eta. \quad (7)$$

The pseudorange errors using the carrier phase measurements are obtained using the difference equation for consecutive epochs as

$$\begin{aligned} \Delta\phi_\rho(t) &= \phi_\rho(t) - \phi_\rho(t-1) \\ &= \delta\rho_I(t) - \delta I(t) + \delta T_r(t) \\ &\quad + \lambda \cdot (N(t) - N(t-1)) + \eta_\phi \\ &= \delta\rho_I(t) - \delta I(t) + \delta T_r(t) + \lambda \cdot \delta N + \eta_\phi. \end{aligned} \quad (8)$$

Here, the integer ambiguity term δN disappears, provided that no cycle slips occur between epochs t and $t - 1$. In case a cycle slip exists, then δN will be reduced by half and can be treated as part of other errors. However, if the time interval between subsequent epochs is kept small enough, the difference equation makes the effect of the cycle slip negligible.

Finally, the new measurement equation for the pseudorange error is modeled by taking the average of (7) and (8) as

$$\frac{\Delta\tau_\rho(t) + \Delta\phi_\rho(t)}{2} = \delta\rho_I(t) + \delta T_r(t) + \frac{\lambda \cdot \delta N}{2} + \frac{\eta + \eta_\phi}{2}. \quad (9)$$

Thus, (9) has no ionospheric effect, while η and η_ϕ get reduced by half. As $T_r(t)$ is usually very small, it can be ignored. Equation (9) becomes the new pseudorange error measurement for the EKF. As mentioned earlier, due to high frequency, the NavIC S-band signal is less prone to ionospheric effects [34]; therefore, in CA-DFVT, we used the estimated carrier phase measurements obtained from the S-band signal. Combine them with the code phase measurements of L5. In this way, the new pseudorange measurement comes out to be less noisy and less erroneous. Thus, the new CA-DFVT pseudorange measurement equation is given as

$$\begin{aligned} z_\tau^i &= \frac{1}{2}[\Delta\tau_\rho^i(t) + \Delta\phi_\rho^i(t)] \\ &= \frac{1}{2}[\Delta\tau^i(t) \cdot \lambda_{L5} + \Delta\phi^i(t) \cdot \lambda_S] \end{aligned} \quad (10)$$

where z_τ^i is the pseudorange error measurement from the i th satellite. λ_{L5} and λ_S are the corresponding wavelengths of L5 and S-band frequencies, respectively. In a discrete time model, $t = t_k$, representing the k th epoch.

Similarly, the pseudorange rate measurement is generated using the Doppler estimate from the carrier discriminator for both the frequencies. Since we use two different frequencies from the same satellite to generate the measurements, an average value of Δf is considered for an accurate measurement and is given as

$$\begin{aligned} z_f^i &= \frac{1}{2}[\Delta f_{\rho,L5}^i(t) + \Delta f_{\rho,S}^i(t)] \\ &= \frac{1}{2}[\Delta f^i(t) \cdot \lambda_{L5} + \Delta f^i(t) \cdot \lambda_S] \end{aligned} \quad (11)$$

where Δf^i in cycles/second is measured by the carrier discriminator for the i th satellite and is expressed as Δf_ρ^i in meters/second. This can also be written in discrete time with $t = t_k$. Based on (10) and (11), the CA-DFVT EKF measurement update equation for M satellites is given as

$$\mathbf{z} = [z_\tau^1, z_\tau^2, \dots, z_\tau^M | z_f^1, z_f^2, \dots, z_f^M]^T_{2M \times 1}. \quad (12)$$

B. Extended Kalman Filter Methodology

For the EKF time update to predict the next state \mathbf{x}_{k+1} , we use a dynamic process noise model [41]. The equations

for the EKF time and measurement update at epoch $k + 1$ are, thus, given as follows:

$$\begin{aligned} \mathbf{x}_{k+1} &= f(\mathbf{x}_k) + w_k \quad w \sim \mathcal{N}(0, \mathbf{Q}) \\ \mathbf{z}_k &= h(\mathbf{x}_k) + v_k \quad v \sim \mathcal{N}(0, \mathbf{R}) \end{aligned} \quad (13)$$

where $f(\cdot)$ and $h(\cdot)$ are known nonlinear functions. \mathbf{Q} is the covariance of the process noise w . It shows the uncertainty in the system model of the EKF and is defined in the CA-DFVT as

$$\mathbf{Q} = \text{diag}[\sigma_x^2 \quad \sigma_y^2 \quad \sigma_z^2 \quad \sigma_{\dot{x}}^2 \quad \sigma_{\dot{y}}^2 \quad \sigma_{\dot{z}}^2 \quad \mathbf{Q}_{clk}]_{8 \times 8} \quad (14)$$

where σ denotes the variance. \mathbf{Q}_{clk} is defined as

$$\mathbf{Q}_{clk} = \begin{bmatrix} S_f \cdot T + \frac{S_g \cdot T^3}{3} & \frac{S_g \cdot T^2}{2} \\ \frac{S_g \cdot T^2}{2} & S_g \cdot T \end{bmatrix} \quad (15)$$

where T is the Kalman filter update interval. S_f and S_g are defined as [42]

$$\begin{aligned} S_f &= c^2 \cdot \frac{h_0}{2} \\ S_g &= c^2 \cdot 2\pi h_{-2} \end{aligned} \quad (16)$$

where h_0 and h_{-2} are called the Allan variances that depend on the type of oscillator used in the receiver. \mathbf{R} is the covariance of the measurement noise v , i.e., the variance in the estimation of the pseudorange and pseudorange rate measurements by the discriminator outputs, and is defined as

$$\mathbf{R} = \text{diag}[\sigma_\rho^1 \dots \sigma_\rho^M | \sigma_\rho^1 \dots \sigma_\rho^M]_{2M \times 2M}. \quad (17)$$

It is to be noted that the discriminator outputs in CA-DFVT represent the pseudorange and pseudorange rate errors; therefore, we choose user position and velocity errors as states and EKF to estimate them. Thus, in CA-DVFT, the state vector $\delta\mathbf{x}$ is given as

$$\begin{aligned} \delta\mathbf{x} &= [\delta x \quad \delta y \quad \delta z \quad \delta \dot{x} \quad \delta \dot{y} \quad \delta \dot{z} \quad b \quad \delta \dot{b}]^T \\ &= [\delta \mathbf{p}^T \quad \delta \mathbf{v}^T \quad b \quad \delta \dot{b}]^T_{8 \times 1} \end{aligned} \quad (18)$$

where b and \dot{b} are the receiver clock time and drift in (meters) and (meters/second), respectively. The discrete time transition matrix propagates the state space model to the next epoch as

$$\begin{aligned} \delta\mathbf{x}_{k+1} &= f(\delta\mathbf{x}_k) \\ &= \Phi \cdot \delta\mathbf{x}_k \end{aligned} \quad (19)$$

where it is assumed that the transition is the steady-state transition matrix that is independent of time (i.e., $\Phi_k = \Phi \forall k$, when steady state is achieved). Hence, the function $f(\cdot)$ is a constant function corresponding to the steady-state transition matrix

$$\Phi = \begin{bmatrix} 0 & 0 & 0 & \Delta t_k & 0 & 0 & 0 & 0 \\ 0 & 0 & 0 & 0 & \Delta t_k & 0 & 0 & 0 \\ 0 & 0 & 0 & 0 & 0 & \Delta t_k & 0 & 0 \\ 0 & 0 & 0 & 0 & 0 & 0 & 0 & 0 \\ 0 & 0 & 0 & 0 & 0 & 0 & 0 & 0 \\ 0 & 0 & 0 & 0 & 0 & 0 & 0 & 0 \\ 0 & 0 & 0 & 0 & 0 & 0 & 1 & \Delta t_k \\ 0 & 0 & 0 & 0 & 0 & 0 & 0 & 0 \end{bmatrix}_{8 \times 8}. \quad (20)$$

The external measurements are related to the state vector by

$$\begin{aligned} \mathbf{z}_k &= \frac{\partial h(\delta \mathbf{x}_{k|k-1})}{\partial \delta \mathbf{x}_{k|k-1}} \cdot \delta \mathbf{x}_{k|k-1} \\ &= \mathbf{H}_k \cdot \delta \mathbf{x}_{k|k-1} \end{aligned} \quad (21)$$

where \mathbf{z} is defined in (12). $\mathbf{H}_k = \mathbf{H}$ is the steady-state observation matrix given as

$$\mathbf{H} = \begin{bmatrix} a_x^1 & a_y^1 & a_z^1 & 0 & 0 & 0 & 1 & 0 \\ \vdots & \vdots \\ a_x^M & a_y^M & a_z^M & 0 & 0 & 0 & 1 & 0 \\ 0 & 0 & 0 & a_x^1 & a_y^1 & a_z^1 & 0 & 1 \\ \vdots & \vdots \\ 0 & 0 & 0 & a_x^M & a_y^M & a_z^M & 0 & 1 \end{bmatrix}_{2M \times 8} \quad (22)$$

The EKF equations for prediction and measurement update, assuming that $\delta \hat{\mathbf{x}}_k^+$ and \mathbf{P}_k^+ are known, are given as follows:

$$\begin{aligned} \delta \hat{\mathbf{x}}_{k+1}^- &= \Phi \cdot \delta \hat{\mathbf{x}}_k^+ \\ \mathbf{P}_{k+1}^- &= \Phi \mathbf{P}_k^+ \Phi^T + \mathbf{Q} \\ \mathbf{K}_{k+1} &= \mathbf{P}_{k+1}^- \mathbf{H}^T (\mathbf{H} \mathbf{P}_{k+1}^- \mathbf{H}^T + \mathbf{R})^{-1} \\ \delta \hat{\mathbf{x}}_{k+1}^+ &= \delta \hat{\mathbf{x}}_{k+1}^- + \mathbf{K}_{k+1} (\mathbf{z}_{k+1} - \mathbf{H} \cdot \delta \hat{\mathbf{x}}_{k+1}^-) \\ \mathbf{P}_{k+1}^+ &= (\mathbf{I} - \mathbf{K}_{k+1} \mathbf{H}) \mathbf{P}_{k+1}^- \end{aligned} \quad (23)$$

where “+” denotes *posterior* (updated), “-” denotes *prior* (predicted) estimate, and \mathbf{P}_0^- and $\delta \hat{\mathbf{x}}_0^-$ are initialized before running the EKF loop.

III. IMPLEMENTATION AND EXPERIMENTAL SETUP

In this section, the implementation and experimental setup are described. Fig. 2 shows the complete functional flow of our CA-DFVT receiver architecture. For initializing the CA-DFVT, the individual ST results, i.e., initial receiver PVT and ephemeris of both L5 and S-band, are considered. In order to maintain high precision, we take the average of the PVT solution obtained from L5 and S-band as a reference input to CA-DFVT.

In CA-DFVT, the residuals i.e., pseudorange error and pseudorange rate extracted from the code and carrier tracking loops, are converted into code and carrier measurements and then used as the measurements of the EKF. Measurements as given in (7) and (8) from L5 and S-band tracking loops are considered. The computed receiver PVT is then utilized to predict the next epoch’s pseudorange, pseudorange rate, and LOS vectors.

A. Experimental Setup

Two different test experiments, i.e., static and dynamic, were conducted to evaluate the performance of our CA-DFVT receiver architecture. The experimental setup and environments for both static and dynamic field tests in this research are shown in Fig. 3. The radio frequency (RF) L5 and S-band C/A signals of NavIC were received through a multiband TTSLVAV-V2 antenna. National Instruments (NI)

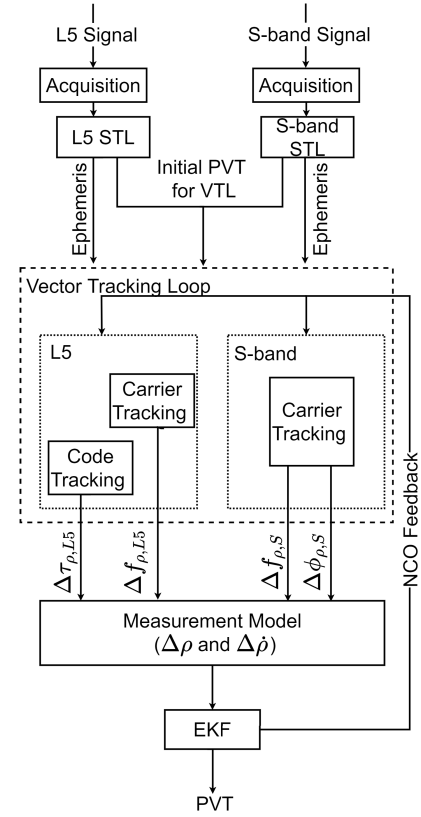


Fig. 2. Flowchart of the proposed CA-DFVT.

universal software radio peripheral (USRP)-2932 devices were used to downconvert these RF NavIC signals to the intermediate frequency (IF). For this purpose, two USRP devices, one for each frequency, were connected together. The USRP devices were synchronized through a multiple-input-multiple-output (MIMO) cable to share the common clock and Ethernet connections. In addition, a high-end ISRO’s in-house IRNSS-GPS-satellite-based augmentation system (SBAS) (IGS) receiver in the multifrequency mode was used as a high-accuracy reference for the test experiments. Using an RF power splitter and several RF cables, the signals from the same antenna were split into the USRP front-end devices and the IGS receiver. Detailed technical specifications and settings of the RF front end are tabulated in Table II.

IV. RESULTS AND DISCUSSION

In this section, the experimental results are discussed in detail for both the test scenarios. In the static test, the NavIC L5 and S-band signals were collected using the permanently mounted antenna on the roof-top building of the Digital Communication Laboratory, Birla Institute of Technology and Science, Pilani, K K Birla Goa Campus, Pilani, India. Since this is an open-sky roof-top location, it is expected that the measurements will be free from surrounding effects, such as multipath and NLOS, but the S-band signal is affected by the nearby Wi-Fi router present in the building. This experiment is to validate the performance of our CA-DFVT receiver architecture in stationary situations where the effects of vehicular

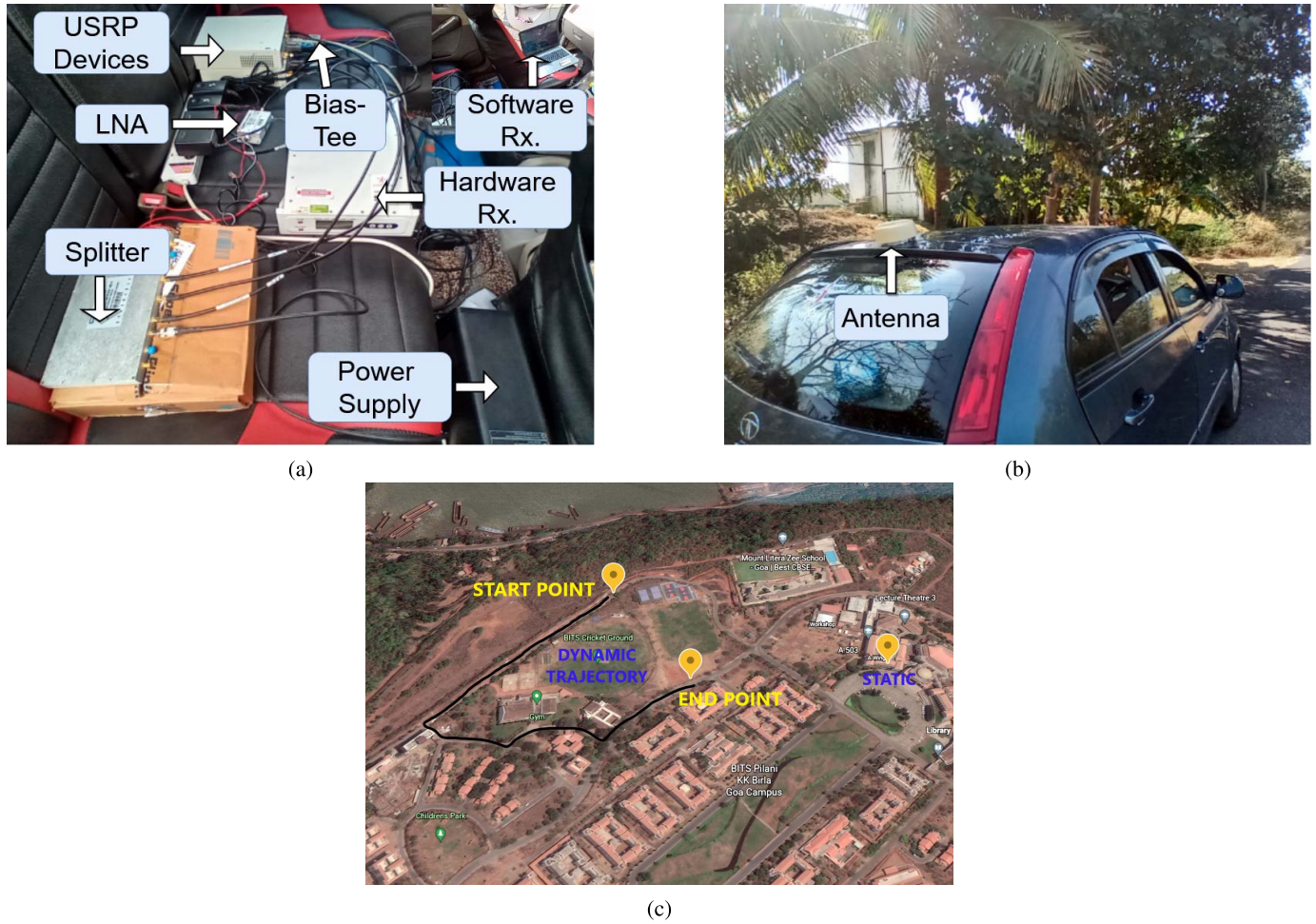


Fig. 3. Experimental setup and environments. (a) Equipment, (b) Receiver antenna, and (c) Dynamic test environments (from Google Earth).

TABLE II
RF FRONT-END TECHNICAL SPECIFICATIONS AND SETTINGS

Equipment	Parameters	Specifications
Antenna	Polarization	TTSLVAV-V2 Right hand circularly polarized (RHCP)
Front-end	Device	NI-USRP 2932
	RF coverage	400 MHz – 4.4 GHz
	Bandwidth	20 KHz – 40 MHz
	ADC Resolution	14-bit
	Oscillator	GPSDO (OCXO), frequency stability : 25 ppb
	Bias-Tee	Range: 10 – 4200 MHz, Low insertion loss: 0.6 dB
	Low noise amplifier	Range: 700 – 3500 MHz, Noise figure: 2.5 dB
	Power splitter	Wide band: 500 – 6000 MHz, Insertion loss: 1.5 dB
	Sampling frequency (f_s)	Static: 10 MHz; Dynamic: 4 MHz
	Intermediate frequency (IF)	0 MHz
GNSS Signal	NavIC L5 and S-band C/A	
Data type and format	Interleaved (I-Q) INT16	

movement of the receiver on clock bias and drift errors are nil. At the same time, signal availability and performance in the equatorial low-latitude region and in the presence of interference are also validated through this experiment.

For the dynamic test conducted on the university campus near the staff residential apartments, the antenna was mounted on the roof of a car. The car was kept static for 80 s before driving with a moderate speed along the trajectory, as shown in Fig. 3(c). The trajectory consists of a total of six sharp bends along with two small inclines. The densely located trees and staff residential apartments significantly hinder signal transmission, resulting in frequent signal disruptions. However, due to the only possible 2-D view of India in Google Earth, the building and tree heights are not visible correctly, but the actual path is densely surrounded by the nearby objects, which includes trees and buildings. This experiment validates the reliability and robustness of the proposed CA-DFVT receiver architecture in the dynamic situation. Detailed result analyses of both static and dynamic test cases are described in the subsequent Sections IV-A and B.

A. Static Test Analysis

In this test, we collected 100 s data for both L5 and S-band sampled at 10 MHz to yield data streams with digital IF at 0 MHz (refer Table II). The signals were processed using the conventional ST. Based on the outcome of the ST, the signals are then processed using VT. In VT, first, we processed

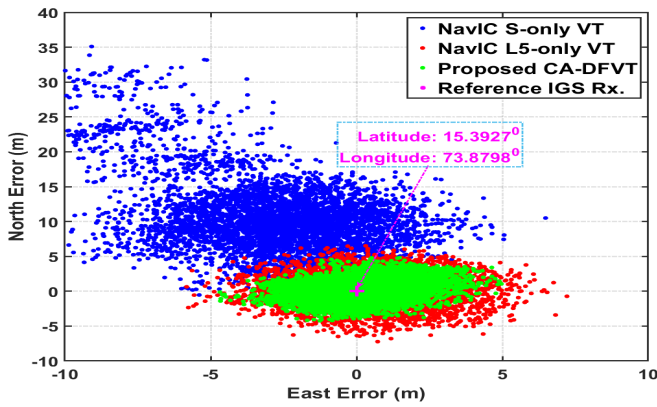


Fig. 4. Horizontal positioning errors in east and north directions for the static test case.

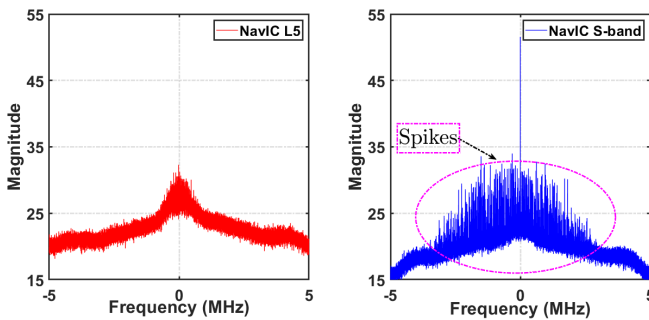


Fig. 5. Frequency spectrum of NavIC L5 and S-band signals during the static case.

both L5 and S-band signals separately in single-frequency architecture. Afterward, both these signals were processed using our CA-DFVT receiver architecture. The horizontal positioning errors in the east and north directions for single-frequency S-only VT, L5-only VT, and proposed CA-DFVT during about 50 s are shown in Fig. 4.

As can be observed in Fig. 4, the positioning error of the proposed CA-DFVT is smaller than the single-frequency VT solutions. The mean and maximum horizontal positioning errors for L5-only VT are 2.729 and 7.629 m, respectively, whereas, for S-only VT, it is 11.450 and 36.344 m, respectively. On the other hand, the mean and maximum horizontal positioning errors for the proposed CA-DFVT are 2.139 and 5.755 m, respectively. Among the three algorithms, the S-only VT has a higher positioning error. This is probably because of the interference from 2.4-GHz unlicensed S-band sources in NavIC signals. In this case, NavIC S-band signals were most likely affected by the nearby Wi-Fi and/or Bluetooth signals present in the university building, which can be confirmed from the frequency spectrum of NavIC S-band, as shown in Fig. 5.

As seen in Fig. 5, several dominant spikes are present in the frequency spectrum within the bandwidth of the NavIC S-band signal, while the L5 signal is clear and smooth. It has been identified that LTE/Bluetooth and Wi-Fi signals were the major sources of interference in this case. From this, it can be inferred that the standalone NavIC S-band is not preferable unless the observations are corrected using additional

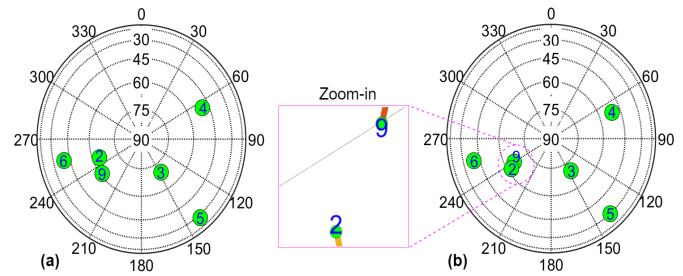


Fig. 6. Sky plots of (a) static and (b) dynamic test cases.

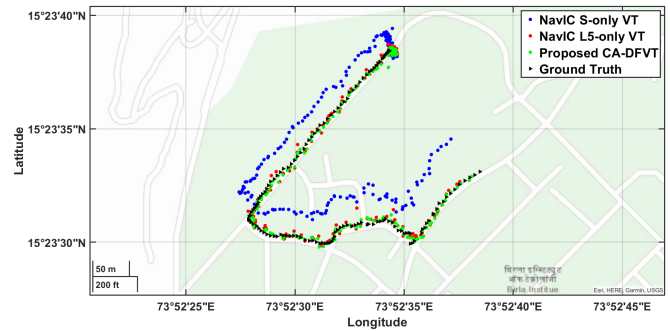


Fig. 7. Geosscatter plot of the positioning results at a 1-s interval in the dynamic test in a semiurban location.

algorithms, as done in [15]. Another possible solution is by combining code and carrier measurements of S-band and L5 as done in the proposed CA-DFVT, thus improving the positioning performance significantly. The overall navigation results of the proposed CA-DFVT are consistent and satisfactory. Moreover, it is evident that satisfactory results can be obtained primarily when the number of visible satellites satisfies the least number of required observations [25]. In the Indian subcontinent, it is most likely that at least seven NavIC satellites are always available with good signal strength unless blocked. For both static and dynamic cases, at least six satellites with a pseudorandom noise (PRN) codes 2, 3, 4, 5, 6, and 9 were visible for the entire test durations. The sky plots of the space vehicles (SVs) during the static and dynamic tests are depicted in Fig. 6(a) and (b), where the zoomed-in part in Fig. 6(b) shows the movement of satellites in the dynamic case.

B. Dynamic Test Analysis

For the dynamic case, the sampling frequency (f_s) and IF of the front end are 4 and 0 MHz, respectively. As mentioned earlier, in this test, for the first 80 s, the car was in an open-sky static condition to ensure that the receiver acquired all the ephemeris, computed the satellite positions, and output stable navigation solutions. Thereafter, the car started moving with a moderate speed of 18–36 km/h. Fig. 7 shows the dynamic positioning results of S-only VT, L5-only VT, proposed CA-DFVT, and IGS reference receiver. The dynamic trajectory was obtained and used as a reference from the best operational mode of the ISRO's IGS receiver (i.e., GPS L1 + Dual NavIC + SBAS). The trajectory of this semiurban canyon was surrounded by trees and buildings along with

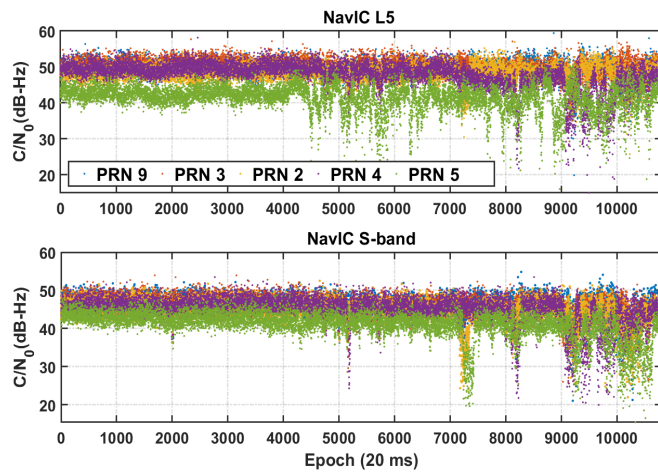


Fig. 8. NavIC L5 and S-band C/N_0 ratios in the dynamic test scenario.

sharp turns on the path from start point to endpoint. Thus, this dynamic trajectory was more susceptible to signal-challenging conditions, such as reduced signal availability, weak signal, and foliage. This can be inferred from the carrier-to-noise ratio (C/N_0) values of tracked satellites in both L5 and S-band signals, which are shown in Fig. 8.

As can be seen in Fig. 8, the satellites encountered a frequent drop in the C/N_0 of both L5 and S-band signals. Mainly, the drop in signal strength got extended as the car started moving through the sharp turns and foliage. It was observed that, during the steep roads around the sharp turns, i.e., 180–290 s, the S-band signal encountered a drop in C/N_0 . However, compared to the S-band, the fluctuations in the L5 signal are more severe, and these fluctuations are present throughout the dynamics.

As observed in Fig. 7, the single-frequency S-only VT has a significant positioning error throughout the trajectory. On the other hand, the L5-only VT and CA-DFVT perform well. The S-only VT shows an offset from the trajectory. Although it is capable of correctly tracing the trajectory, including the turns, the positioning results are shifted away from the true path. This offset can probably be due to the relative positioning of VT because the positioning performance of the VT depends upon the initial estimates of PVT and ephemeris information from the ST. Furthermore, the corresponding pseudoranges from the S-band signal could also be a possible reason for disrupting the VT’s performance, as S-band signals are interfered with by the out-of-band interference. The single-frequency L5 VT, on the other hand, performs well, but the positioning inaccuracy increases during the sharp bends and steep road conditions. However, our CA-DFVT has a lower positioning error compared to the other two methods. CA-DFVT is able to provide more precise and accurate positioning. This improvement in positioning is achieved due to the usage of more precise carrier phase measurements from the S-band. Combine them with the code phase measurements of the L5-band, which are free from interference as per the signal properties. Thus, the new measurements formulated from both resulted in lower positioning errors in high dynamics.

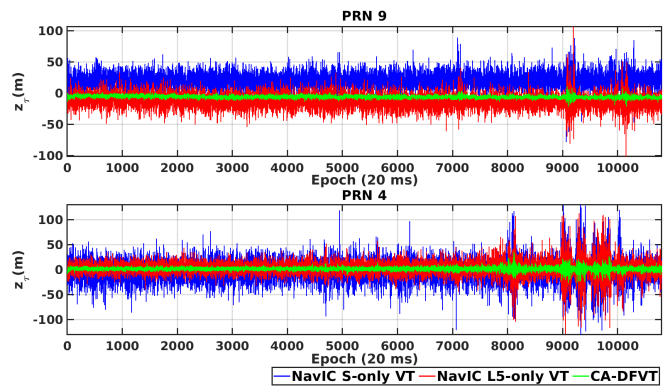


Fig. 9. Estimated pseudorange measurement errors for the dynamic test.

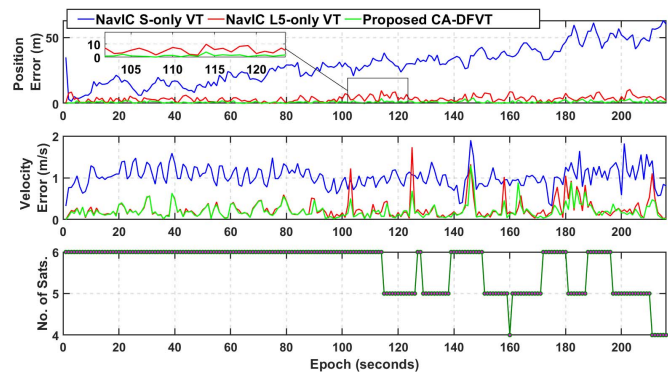


Fig. 10. Navigation solution errors for the dynamic test case.

The estimated pseudorange measurements of L5-only VT, S-only VT, and the proposed CA-DFVT of PRNs 4 and 9 are compared in Fig. 9. As can be observed, the CA-DFVT has lower measurement values than L5-only VT and S-only VT, which implies less pseudorange error. As expected, the pseudorange measurement is smooth during the static situation, while, as the car moves, the impact of dynamics can be clearly seen and is consistent with the C/N_0 , as shown in Fig. 8. Furthermore, the variations in the pseudorange measurements for L5-only VT and S-only VT are noisier, but they are significantly smoother in our CA-DFVT. This improvement in CA-DFVT is a result of the new measurement model.

Fig. 10 shows the navigation results of S-only VT, L5-only VT, and the proposed CA-DFVT. We can observe that the maximum positioning error of S-only VT is nearly 63 m, whereas, for L5-only VT and CA-DFVT, it remains below 10 m. In the case of S-only VT, the positioning error is low ~ 15 m in the starting but gradually gets higher and reaches up to ~ 63 m as the dynamic changes. This increase in error is observed in the velocity of S-only VT as well, where the velocity error increases gradually along the trajectory. Also, the large initial error in S-only VT is due to the ST results used to initialize the VT.

On the other hand, except during the sharp bends and steep roads, not many variations are observed in velocity error of L5-only VT and CA-DFVT. However, there is at least a 4–5-m difference in the positioning and velocity error

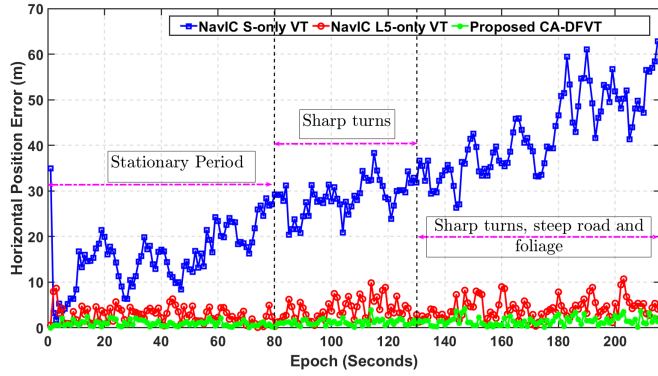


Fig. 11. Horizontal position error for the NavIC S-only VT, NavIC L5-only VT, and proposed CA-DFVT under the dynamic test case.

TABLE III
HORIZONTAL POSITIONING ERROR IN DIFFERENT PERIODS
DURING THE DYNAMIC TEST

Period	NavIC S-only VT			NavIC L5-only VT			Proposed CA-DFVT		
	Max (m)	Mean (m)	Standard deviation (m)	Max (m)	Mean (m)	Standard deviation (m)	Max (m)	Mean (m)	Standard deviation (m)
1 (1–80 s)	34.9506	15.9281	6.6650	8.6551	2.8134	1.7678	2.3595	0.9421	0.5892
2 (81–130 s)	38.3409	28.6558	3.8620	9.8434	3.9969	2.2840	3.8746	1.1940	0.6292
3 (131–216 s)	62.8030	42.9158	8.8742	10.6968	4.1788	2.2081	4.1538	1.4734	0.9310

between L5-only VT and CA-DFVT. Moreover, the velocity and position error plots are consistent with the number of satellites in view of the receiver in each epoch. As the number of satellites goes down, the positioning error of S-only VT and L5-only VT increases. However, in the case of our CA-DFVT, the positioning error does not increase much. The horizontal positioning errors for these three algorithms are quantitatively provided in Table III. The analysis is divided into three parts, where the first part corresponds to the stationary period (1–80 s), while the second period (81–130 s) includes few sharp bends and steep road conditions. The third period (131–216 s) is a mixture of sharp turns, steep road, and foliage due to nearby trees and buildings, as shown in Fig. 11. Overall, the proposed CA-DFVT outperforms the single-frequency NavIC S-only and L5-only VT algorithms.

Fig. 12 shows the frequency results of PRN 4 for both L5 and S-band channels; other channels have similar results and are not listed here. As seen in Fig. 12, all three algorithms are able to provide frequency results. However, compared to L5-only VT and CA-DFVT, the S-only VT shows a similar offset as seen in positioning error. The overall trend of the frequency estimates is the same but with offset. Furthermore, the difference between L5-only and CA-DFVT is small, but the overall variance of CA-DFVT is lower. The estimates of L5-only VT become noisier, especially during periods 2 and 3 in the dynamics.

Fig. 13 shows the velocity estimations through different algorithms. As per the dynamics, the car was stationary for the first 80 s. Once the car started moving, the maximum absolute velocities in the east and north during 81–216 s were

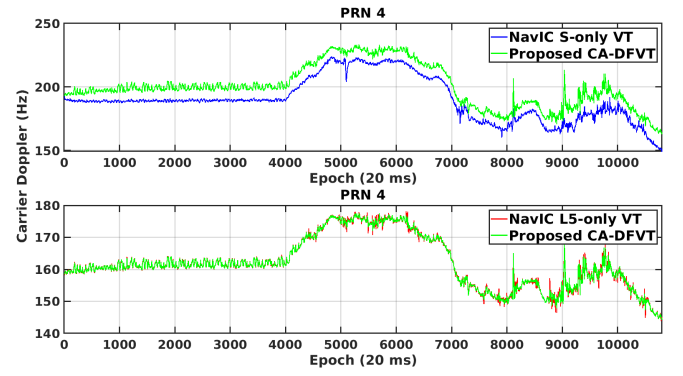


Fig. 12. NavIC L5 and S-band carrier Doppler frequencies in the semiurban area under the dynamic test case.

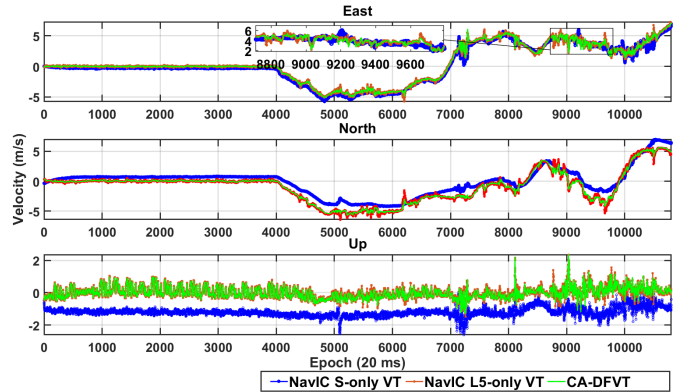


Fig. 13. Velocity estimations for the dynamic test scenario.

approximately 7.15 and 5.76 m/s, respectively. As can be seen, the S-only VT fails to estimate the velocities accurately in the north and up directions. Moreover, as seen in positioning results, a similar offset was observed during the velocity estimations as well. A zoomed-in portion is displayed in Fig. 13 (top), where the difference in the velocity estimation in the east direction by different algorithms can be observed. A similar trend is also observed in north and up directions. Among these algorithms, the CA-DFVT estimates more precise and accurate velocity in the east, north, and up directions.

V. CONCLUSION

NavIC utilizes L5 and S-band signals for navigation solutions. Each of these frequency bands has its own merits and demerits in terms of signal properties, such as the S-band signal's less ionospheric delay and carrier phase noise, and the L5 signal's inherent noise mitigation capabilities. A single-frequency NavIC receiver architecture in VT is susceptible to NavIC signal tracking and positioning degradation under challenging environments. To increase the reliability and robustness of NavIC signal tracking and positioning, we proposed CA-DFVT. CA-DFVT jointly tracks NavIC L5 and S-band signals and estimates position using the new measurements, where the carrier phase measurements from the S-band were combined with the code-phase measurements of L5. This is the first of its type where carrier phase measurements from a different frequency band, i.e., S-band having a high frequency,

are utilized to formulate a new pseudorange measurement for the EKF in the dual-frequency mode. We experimentally demonstrated the performance of the proposed CA-DFVT in terms of reliability and robustness under weak signal, high dynamics, interference, and failure of single-frequency NavIC VT algorithms.

As future work, a possible extension of this work is to perform a detailed performance analysis of CA-DFVT under other challenging conditions that are not covered in present work, such as under ionospheric scintillation, strong multipath, and NLOS.

APPENDIX DERIVATION OF EQUATION (3)

A mathematical model is described here, which relates the user's position and velocity errors to the code phase and carrier frequency errors output by the code and carrier discriminators. The main focus is on carrier frequency error; however, the same derivation can be carried out for the code phase as well [43]. The receiver clock time $T_r(t)$ is defined as

$$\begin{aligned} T_r(t) &= \frac{(\phi(t) - \phi_0)}{f_{\text{carr}}} \\ \phi(T_r) &= f_{\text{carr}} \cdot T_r + \phi_0 \end{aligned} \quad (\text{A.1})$$

where $\phi(t)$ is the phase at time t , $\phi_0 = \phi(0)$ is the phase at $t = 0$, f_{carr} is the carrier frequency, and $\phi(T_r)$ is the phase when synchronized with the receiver clock.

Note that, when the GNSS signal is received, it gets multiplied by the local signal and a beat frequency is produced. Thus, the carrier phase that is output by the carrier discriminator for the j th satellite, $\Phi^j(T_r)$, is the phase difference that is given as [44]

$$\Phi^j(T_r) = \phi(T_r) - \phi^j(T_r) - N^j \quad (\text{A.2})$$

where $\phi^j(T_r)$ is the carrier phase at the transmission time from the j th satellite that has been synchronized with the receiver clock and $\phi(T_r)$ is the carrier phase from the locally generated replica. N^j is the integer phase ambiguity for the j th satellite. Substituting the value of $\phi(T)$ in (A.2) gives

$$\begin{aligned} \Phi^j(T_r) &= f_{\text{carr}} \cdot T_r + \phi_0 - f_{\text{carr}} \cdot T_r^j - \phi_0^j - N^j \\ &= f_{\text{carr}} \cdot (T_r - T_r^j) + (\phi_0 - \phi_0^j - N^j) \\ &= f_{\text{carr}} \cdot (T_r - T_r^j) + \Gamma \end{aligned} \quad (\text{A.3})$$

where $\Gamma = (\phi_0 - \phi_0^j - N^j)$ is constant. Φ^j is in rad/s, which is converted to meters so that it can be related to pseudorange before it is fed as input to the EKF in the measurement vector \mathbf{z} . This is done as follows:

$$\begin{aligned} \Phi_\rho^j(T_r) &= \frac{c}{f_{\text{carr}}} \cdot \Phi^j(T_r) \\ &= \frac{c}{f_{\text{carr}}} \cdot (f_{\text{carr}} \cdot (T_r - T_r^j) + \Gamma) \\ &= c \cdot (T_r - T_r^j) + \frac{c}{f_{\text{carr}}} \cdot \Gamma \end{aligned} \quad (\text{A.4})$$

where Φ_ρ^j is the carrier phase in meter for the j th satellite. Then, the simplified pseudorange equation is modeled as

$$\begin{aligned} \rho^j &= c \cdot (T_r - T_r^j) \\ &= R + b + \epsilon \end{aligned} \quad (\text{A.5})$$

where R is the geometric distance between the user and j th satellite given by

$$R = \sqrt{(x - x^j)^2 + (y - y^j)^2 + (z - z^j)^2}. \quad (\text{A.6})$$

b is the receiver clock bias in m, and ϵ includes all the errors, such as troposphere, ionosphere, and multipath. From (A.4) and (A.5), the carrier phase can be related to the pseudorange as

$$\Phi_\rho^j(T) = R + b + \epsilon + \lambda_{\text{carr}} \cdot \Gamma. \quad (\text{A.7})$$

Since this is the absolute phase, the phase error is then given by

$$\delta\Phi_\rho^j(T) = \delta R + \delta b + \epsilon + \lambda_{\text{carr}} \cdot \Gamma. \quad (\text{A.8})$$

As mentioned previously, the carrier discriminator output, Δf , is multiplied by λ_{carr} and converted in m/s, which is then related to the receiver velocity as follows:

$$\begin{aligned} \Delta f_\rho &= \lambda_{\text{carr}} \cdot \Delta f \\ &= \lambda_{\text{carr}} \cdot \frac{d(\delta\Phi^j(T))}{dt} \\ &= \frac{d(\lambda_{\text{carr}} \cdot \delta\Phi^j(T))}{dt} \\ &= \frac{d(\delta\Phi_\rho^j(T))}{dt} \\ &= \frac{d(\delta R + \delta b + \epsilon + \lambda_{\text{carr}} \cdot \Gamma)}{dt}. \end{aligned} \quad (\text{A.9})$$

Noting that $\delta R = \delta \mathbf{x}^T \mathbf{a}^j$, and substituting it into (A.9) gives

$$\begin{aligned} \Delta f_\rho &= \frac{d(\delta \mathbf{x}^T \mathbf{a}^j + \delta b + \epsilon + \lambda_{\text{carr}} \cdot \Gamma)}{dt} \\ &= \delta \mathbf{v}^T \mathbf{a}^j + \delta \dot{b} + \text{error}. \end{aligned} \quad (\text{A.10})$$

Although this derivation has been done for the continuous time case, the same holds also for discrete time, where t is replaced by the time index t_k . Equation (A.10) is now consistent with (3).

A similar derivation can now be carried out for the case of the output given by the code discriminator. The autocorrelation for the discriminator is defined as given in [45]

$$R(\tau) = \begin{cases} 1, & -|\tau| \leq |\tau| \leq 1 \\ 0, & \text{otherwise} \end{cases} \quad (\text{A.11})$$

where τ is the code phase error estimated by the receiver in chips. Using a simplified formulation for the Early and Late functions used in the normalized early minus late correlator [8], [46]

$$\begin{aligned} E &= A \cdot R\left(\tau - \frac{d}{2}\right) \\ L &= A \cdot R\left(\tau + \frac{d}{2}\right) \end{aligned} \quad (\text{A.12})$$

where d is the correlator spacing and A is the signal amplitude. As shown in [8], the code discriminator output can be approximated as

$$\Delta\tau = -\frac{\tau}{T_{\text{code}}}, \quad |\tau| \leq \frac{T_{\text{code}}}{2}. \quad (\text{A.13})$$

T_{code} is the code period per chip in seconds. For one code period, T_{code} can be removed from the denominator to get units of chips. To convert this in meter, the approach used for carrier phase above can be implemented

$$\Delta\tau_p = \Delta\tau \cdot \frac{c}{f_{\text{code}}} \quad (\text{A.14})$$

where $\Delta\tau_p$ is the code phase delay in meters and $f_{\text{code}} = (1/T_{\text{code}})$ (chips/s) is the code frequency. Since $\Delta\tau$ is the code phase error, it can also be thought of having the form $f_{\text{code}} \cdot (T - T^j + \Gamma)$, as given in (A.4). The rest of the proof can be followed in a similar way as is done for the carrier discriminator output. Hence, $\Delta\tau_p = \delta R + \delta b + \epsilon$. Since $\delta R = \delta \mathbf{x}^T \cdot \mathbf{a}^j$ as mentioned previously, substituting the value of δR completes the proof.

ACKNOWLEDGMENT

The Universal Software Radio Peripheral (USRP)-2932 devices used as radio frequency (RF) front end in this work were purchased under the contingency fund of the Indian Space Research Organisation (ISRO) Research Sponsored (RESPOND) Project under Grant ISRO/RES/3/720/2016-17.

REFERENCES

- [1] A. Dey, L. M. Joshi, R. Chhibba, and N. Sharma, "A study of ionospheric effects on IRNSS/NavIC positioning at equatorial latitudes," *Adv. Space Res.*, vol. 68, no. 12, pp. 4872–4883, Dec. 2021. [Online]. Available: <https://www.sciencedirect.com/science/article/pii/S0273117720306852>
- [2] S. Das, S. Datta, and A. K. Shukla, "Detection of thunderstorm using Indian navigation satellite NavIC," *IEEE Trans. Geosci. Remote Sens.*, vol. 58, no. 5, pp. 3677–3684, May 2020.
- [3] C. C. R. Garcez *et al.*, "Tensor-based subspace tracking for time-delay estimation in GNSS multi-antenna receivers," *Sensors*, vol. 19, no. 23, p. 5076, Nov. 2019.
- [4] Z. Sun, X. Wang, S. Feng, H. Che, and J. Zhang, "Design of an adaptive GPS vector tracking loop with the detection and isolation of contaminated channels," *GPS Solutions*, vol. 21, no. 2, pp. 701–713, 2016.
- [5] Luo *et al.*, "Research on time-correlated errors using Allan variance in a Kalman filter applicable to vector-tracking-based GNSS software-defined receiver for autonomous ground vehicle navigation," *Remote Sens.*, vol. 11, no. 9, p. 1026, Apr. 2019.
- [6] H. Nourmohammadi and J. Keighobadi, "Decentralized INS/GNSS system with MEMS-grade inertial sensors using QR-factorized CKF," *IEEE Sensors J.*, vol. 17, no. 11, pp. 3278–3287, Jun. 2017.
- [7] B. Xu and L.-T. Hsu, "Open-source MATLAB code for GPS vector tracking on a software-defined receiver," *GPS Solutions*, vol. 23, no. 2, pp. 1–9, Apr. 2019.
- [8] B. Xu, Q. Jia, and L.-T. Hsu, "Vector tracking loop-based GNSS NLOS detection and correction: Algorithm design and performance analysis," *IEEE Trans. Instrum. Meas.*, vol. 69, no. 7, pp. 4604–4619, Jul. 2020.
- [9] M. Lashley, D. M. Bevely, and J. Y. Hung, "Performance analysis of vector tracking algorithms for weak GPS signals in high dynamics," *IEEE J. Sel. Topics Signal Process.*, vol. 3, no. 4, pp. 661–673, Aug. 2009.
- [10] F. M. G. Sousa and F. D. Nunes, "Performance analysis of a VDFLL GNSS receiver architecture under ionospheric scintillation and multipath conditions," in *Proc. IEEE/ION Position, Location Navigat. Symp. (PLANS)*, May 2014, pp. 602–611.
- [11] H. Y. F. Elghamrawy, M. Tamazin, and A. Noureldin, "Investigating the benefits of vector-based GNSS receivers for autonomous vehicles under challenging navigation environments," *Signals*, vol. 1, no. 2, pp. 121–137, Oct. 2020.
- [12] D. D. Jagiwal and S. N. Shah, "Impact of Wi-Fi interference on NavIC signal," *Curr. Sci.*, vol. 114, no. 11, pp. 2273–2280, 2018.
- [13] U. Ghosh, "An empirical performance study of IRNSS S-band signals under Bluetooth interference," in *Proc. URSI Asia-Pacific Radio Sci. Conf. (AP-RASC)*, Mar. 2019, pp. 1–3.
- [14] I. Mateu *et al.*, "Exploration of possible GNSS signals in S-band," in *Proc. 22nd Int. Tech. Meeting Satell. Division Inst. Navigat. (ION GNSS)*, 2009, pp. 1573–1587.
- [15] A. Dey, K. Iyer, and N. Sharma, "S-band interference detection and mitigation using a vector tracking-based NavIC software receiver," in *Proc. 34th Int. Tech. Meeting Satell. Division Inst. Navigat. (ION GNSS+)*, Oct. 2021, pp. 3464–3476.
- [16] J. J. Spilker, Jr., P. Axelrad, B. W. Parkinson, and P. Enge, *Global Positioning System: Theory and Applications*, vol. 1. Washington, DC, USA: American Institute of Aeronautics and Astronautics, 1996, ch. 7.
- [17] S. Chen and Y. Gao, "Improvement of carrier phase tracking in high dynamics conditions using an adaptive joint vector tracking architecture," *GPS Solutions*, vol. 23, no. 1, pp. 1–10, Jan. 2019.
- [18] A. Jafarnia-Jahromi, T. Lin, A. Broumandan, J. Nielsen, and G. Lachapelle, "Detection and mitigation of spoofing attacks on a vector based tracking GPS receiver," in *Proc. 2012 Int. Tech. Meeting Inst. Navigat.*, 2012, pp. 790–800.
- [19] S. Zhao and D. Akos, "An open source GPS/GNSS vector tracking loop-implementation, filter tuning, and results," in *Proc. 2011 Int. Tech. Meeting The Inst. Navigat.*, 2011, pp. 1293–1305.
- [20] K. Borre, D. M. Akos, N. Bertelsen, P. Rinder, and S. H. Jensen, *A Software-Defined GPS and Galileo Receiver: A Single-Frequency Approach*. Cham, Switzerland: Springer, 2007.
- [21] N. Nadarajah, A. Khodabandeh, and P. J. G. Teunissen, "Assessing the IRNSS L5-signal in combination with GPS, galileo, and QZSS L5/E5a-signals for positioning and navigation," *GPS Solutions*, vol. 20, no. 2, pp. 289–297, Apr. 2016.
- [22] M. Z. H. Bhuiyan, S. Honkala, S. Soderholm, and H. Kuusniemi, "Performance analysis of a multi-GNSS receiver in the presence of a commercial jammer," in *Proc. Int. Assoc. Inst. Navigat. World Congr. (IAIN)*, Oct. 2015, pp. 1–6.
- [23] Y. Luo, Y. Wang, and Y. Ma, "Performance analysis of adaptive vector tracking loop," in *Proc. IEEE 11th Int. Conf. Signal Process. (ICSP)*, vol. 3, Oct. 2012, pp. 2166–2170.
- [24] A. Tabatabaei, M. R. Mosavi, H. S. Shahhoseini, and K. Borre, "Vectorized and federated software receivers combining GLONASS and GPS," *GPS Solutions*, vol. 21, no. 3, pp. 1331–1339, Jul. 2017.
- [25] A. Tabatabaei and M.-R. Mosavi, "Performance analysis of GLONASS integration with GPS vectorised receiver in urban canyon positioning," *Surv. Rev.*, vol. 51, no. 368, pp. 460–471, Sep. 2019.
- [26] E. Shytermeja, "Design and performance of a GNSS single-frequency multi-constellation vector tracking architecture for urban environments," Ph.D. dissertation, Signal Image Process., INPT, Toulouse, France, 2017.
- [27] E. Shytermeja, A. J. G. Pena, and O. Julien, "Dual-constellation vector tracking algorithm in ionosphere and multipath conditions," in *Proc. 4th Int. Tech. Symp. Navigat. Timing (ITSNT)*, Toulouse, France, Nov. 2017.
- [28] S. A. Nik and M. Petovello, "Implementation of a dual-frequency GLONASS and GPS L1 C/A software receiver," *The J. Navigat.*, vol. 63, no. 2, p. 269, 2010.
- [29] J. T. Curran, M. Petovello, and G. Lachapelle, "Design paradigms for multi-constellation multi-frequency software GNSS receivers," in *Proc. China Satell. Navigat. Conf. (CSNC)*. Cham, Switzerland: Springer, 2013, pp. 751–765.
- [30] E. Shytermeja, A. Garcia-Pena, and O. Julien, "Performance comparison of a proposed vector tracking architecture versus the scalar configuration for a L1/E1 GPS/galileo receiver," 2019, [arXiv:1905.11022](https://arxiv.org/abs/1905.11022).
- [31] S. Zaminpardaz, P. J. G. Teunissen, and N. Nadarajah, "IRNSS/NavIC and GPS: A single- and dual-system I5 analysis," *J. Geodesy*, vol. 91, no. 8, pp. 915–931, Aug. 2017.
- [32] L. Lau, H. Tateshita, and K. Sato, "Impact of multi-GNSS on positioning accuracy and multipath errors in high-precision single-epoch solutions—A case study in ningbo China," *J. Navigat.*, vol. 68, no. 5, pp. 999–1017, Sep. 2015.
- [33] D. V. Ratnam, T. R. Vishnu, and P. B. S. Harsha, "Ionospheric gradients estimation and analysis of S-band navigation signals for NAVIC system," *IEEE Access*, vol. 6, pp. 66954–66962, 2018.

- [34] K. Praveena, P. N. Kumar, D. K. Reddy, and N. Santhosh, "Analysis of ionospheric scintillations of NavIC L₅ and S-band signals over low latitude Indian region," *Proc. Comput. Sci.*, vol. 171, pp. 989–998, Jan. 2020.
- [35] B. M. Ledvina, M. L. Psiaki, D. Sheinfeld, A. P. Cerruti, S. P. Powell, and P. M. Kintner, "A real-time GPS civilian L₁/L₂ software receiver," in *Proc. 17th Int. Tech. Meeting Satell. Division The Inst. Navigat. (ION GNSS)*, 2004, pp. 986–1005.
- [36] J. Klobuchar, "Ionospheric time-delay algorithm for single-frequency GPS users," *IEEE Trans. Aerosp. Electron. Syst.*, vol. AES-23, no. 3, pp. 325–331, May 1987.
- [37] T. Rethika, S. Mishra, S. Nirmala, S. Rathnakara, and A. Ganeshan, "Single frequency ionospheric error correction using coefficients generated from regional ionospheric data for IRNSS," *Indian J. Radio Space Phys.*, vol. 42, no. 3, pp. 125–130.
- [38] N. Linty, "Snapshot estimation algorithms for GNSS mass-market receivers," Ph.D. dissertation, Ingegneria Elettronica Delle Comunicazioni-XXVII Ciclo, Politecnico di Tori, Turin, Italy, 2015.
- [39] S. Bhattacharyya, "Performance and integrity analysis of the vector tracking architecture of GNSS receivers," Ph.D. dissertation, Dept. Aerosp. Eng. Mech., Univ. Minnesota, Minneapolis, MN, USA, 2012.
- [40] Y. J. Morton, F. van Diggelen, J. J. Spilker, Jr., B. W. Parkinson, S. Lo, and G. Gao, *Position, Navigation, and Timing Technologies in the 21st Century: Integrated Satellite Navigation, Sensor Systems, and Civil Applications*. Hoboken, NJ, USA: Wiley, 2021.
- [41] D. Simon and T. L. Chia, "Kalman filtering with state equality constraints," *IEEE Trans. Aerosp. Electron. Syst.*, vol. 38, no. 1, pp. 128–136, Jan. 2002.
- [42] M. V. Lashley, S. Martin, and J. Sennott, "Vector processing," in *Vector Processing (Position, Navigation, and Timing Technologies in the 21st Century: Integrated Satellite Navigation, Sensor Systems, and Civil Applications)*, vol. 1. Hoboken, NJ, USA: Wiley, 2020, ch. 6, pp. 377–418.
- [43] G. Blewitt, "Basics of GPS technique: Observation equations," in *Geodetic Applications of GPS (Lecture Notes for Nordic Autumn School)*. Båstad, Sweden: Nordic Geodetic Commission, Aug. 1996, pp. 26–31.
- [44] P. D. Groves, "Principles of GNSS, inertial, and multisensor integrated navigation systems, 2nd edition [book review]," *IEEE Aerosp. Electron. Syst. Mag.*, vol. 30, no. 2, pp. 26–27, Feb. 2015.
- [45] W. Nam and S.-H. Kong, "Least-squares-based iterative multipath super-resolution technique," *IEEE Trans. Signal Process.*, vol. 61, no. 3, pp. 519–529, Feb. 2013.
- [46] A. J. van Dierendonck, P. Fenton, and T. Ford, "Theory and performance of narrow correlator spacing in a GPS receiver," *Navigation*, vol. 39, no. 3, pp. 265–283, Sep. 1992.



Abhijit Dey (Member, IEEE) received the B.E. degree from the Department of Electronics and Communication Engineering, Kavayitri Bahinabai Chaudhari Kavayitri Bahinabai Chaudhari North Maharashtra University, Jalgaon, India, in 2011, and the master's degree in radio frequency and microwave engineering in 2014. He is currently pursuing the Ph.D. degree with the Department of Electrical and Electronics Engineering, Birla Institute of Technology and Science, Pilani, India.

He was a Junior Research Fellow with the Birla Institute of Technology and Science. He is currently a Visiting Ph.D. Researcher with the Department of Aeronautical and Aviation Engineering, The Hong Kong Polytechnic University, Hong Kong, SAR, China. His research interests include signal processing in software-defined global navigation satellite system (GNSS) receivers, interference, and ionospheric scintillation detection and mitigation techniques for GNSS systems.



Kaushik Iyer received the B.E. degree from the Department of Electrical and Electronics Engineering, Birla Institute of Technology and Science, Pilani, India, in 2021. He is currently pursuing the master's degree with the Department of Electrical Engineering, Arizona State University, Tempe, AZ, USA.

He was a Research Assistant with the Space Systems Laboratory (SSL), Indraprastha Institute of Information Technology (IIIT-Delhi), New Delhi, India, from June to December 2021. His research interests include nonlinear control theory, adaptive signal processing, and Bayesian estimation with applications in space navigation, autonomous systems, and robotics.



software-defined global navigation satellite system receivers.

Bing Xu (Member, IEEE) received the B.S. and Ph.D. degrees in network engineering and navigation guidance and control from the Nanjing University of Science and Technology, Nanjing, China, in 2012 and 2018, respectively.

He was a Post-Doctoral Fellow with the Department of Aeronautical and Aviation Engineering, The Hong Kong Polytechnic University, Hong Kong, SAR, China, from 2019 to 2020, where he is currently a Research Assistant Professor. His current research interest includes signal processing in



Nitin Sharma received the Ph.D. degree from the Birla Institute of Technology and Science (BITS), Pilani, India, in 2014. His research dissertation is in wireless communication.

He is currently an Associate Professor with the Department of Electrical and Electronics Engineering (EEE), BITS Pilani, K K Birla Goa Campus, Pilani. He is also working in the area of global navigation satellite system (GNSS) signal processing. He is also working on a consultancy project related to sensor networks and signal processing funded by Underwater range (UWR), Defence Research and Development Organization (DRDO) Goa. Apart from these projects, he is also working on a project funded by the Melinda & Gates Foundation in the field of wastewater management. He is responsible for sensor data transmission, analysis, and control in this project. He is also responsible for developing Android/web-based applications for sensor data collection and display. He is also guiding six Ph.D. scholars in the field of wireless communication and signal processing. He has more than 15 publications in peer-reviewed journals in the area of optimization in wireless data transmission. His current research interests include optimization in wireless communication, resource allocation and management for wireless and wired communications, cognitive radio, green communication technologies, machine to machine (M2M)/Internet-of-Things (IoT) communications, cloud communication, and evolutionary computations.

Dr. Sharma is also serving as a Technical Program Committee (TPC) Member for prestigious IEEE conferences, such as IEEE International Conference on Communications (ICC) and IEEE Global Communications Conference (GLOBECOM). He is also a Principal Investigator of a funded project from the Indian Space Research Organisation (ISRO) in GNSS signal processing. He also serves as an Associate Editor for three international journals and has been an Active Reviewer for many journals, including IEEE TRANSACTIONS ON EVOLUTIONARY COMPUTATION (TEC), IEEE SYSTEMS JOURNAL, *Computers & Electrical Engineering* (Elsevier), *Information Sciences*, *Computers & Electrical Engineering*, *Wireless Personal Communications* (Springer), and *Frontiers of Computer Science*.



Li-Ta Hsu (Member, IEEE) received the B.S. and Ph.D. degrees in aeronautics and astronautics from National Cheng Kung University, Tainan, Taiwan, in 2007 and 2013, respectively.

He was a Post-Doctoral Researcher with the Institute of Industrial Science, The University of Tokyo, Tokyo, Japan. In 2012, he was a Visiting Scholar with the Faculty of Engineering, University College London, London, U.K. He is currently an Associate Head and Associate Professor with the Department of Aeronautical and Aviation Engineering, The

Hong Kong Polytechnic University, Hong Kong, SAR, China. His current research interests include global navigation satellite system positioning in challenging environments and localization for autonomous driving vehicles and unmanned aerial vehicles.

Dr. Hsu has been an Associate Fellow of the Royal Institute of Navigation (RIN) and a Council Member of the Institute of Navigation (ION) since 2019.